Recent Progress on Air-bearing Slumping of Segmented Thin-shell Mirrors for x-ray Telescopes: Experiments and Numerical Analysis

Heng E. Zuo[a], Youwei Yao[b], Brandon D. Chalifoux[c], Michael D. DeTienne[d], Ralf K. Heilmann[b], Mark L. Schattenburg[b]

[a]MIT Dept. of Aeronautics & Astronautics Engineering, Cambridge, MA, USA 02139
[b]Space Nanotechnology Lab, MIT Kavli Institute, Cambridge, MA, USA 02139
[c]MIT Dept. of Mechanical Engineering, Cambridge, MA, USA 02139
[d]Izentis LLC, Cambridge, MA, USA 02139

ABSTRACT

Slumping (or thermal-shaping) of thin glass sheets onto high precision mandrels was used successfully by NASA Goddard Space Flight Center to fabricate the NuSTAR telescope. But this process requires long thermal cycles and produces mid-range spatial frequency errors due to the anti-stick mandrel coatings. Over the last few years, we have designed and tested non-contact horizontal slumping of round flat glass sheets floating on thin layers of nitrogen between porous air-bearings using fast position control algorithms and precise fiber sensing techniques during short thermal cycles.

We recently built a finite element model with ADINA to simulate the viscoelastic behavior of glass during the slumping process. The model utilizes fluid-structure interaction (FSI) to understand the deformation and motion of glass under the influence of air flow. We showed that for the 2D axisymmetric model, experimental and numerical approaches have comparable results. We also investigated the impact of bearing permeability on the resulting shape of the wafers. A novel vertical slumping set-up is also under development to eliminate the undesirable influence of gravity. Progress towards generating mirrors for good angular resolution and low mid-range spatial frequency errors is reported.

Keywords: x-ray mirrors, slumping, air-bearing, fluid-structure interaction, viscoelastic, deformation

1. INTRODUCTION

1.1 Motivation and goals

The main motivation for x-ray observatory development is to probe answers to a number of key questions in astronomy, such as to "discover how the universe works, explore how it began and evolved, and search for life on planets around other stars" as NASA's strategic objective states.[1] By projecting humankind's vantage point into space with observatories in Earth orbit and deep space, we seek to understand these profound topics about the universe. More details are described in both the Decadal Survey of Astronomy and Astrophysics performed by National Research Council[2] and the NASA Astrophysics Roadmap.[3]

Future x-ray astronomy observations call for x-ray telescopes with both fine angular resolution and large effective areas. Different missions have various requirements depending on the energy band of the x-ray sources of interest, yet all of them will benefit from the development of lightweight high resolution thin-shell mirrors. Typically, the ideal angular resolution requires $0.5-5$ arcsecond HPD in the sub 1 keV band with collecting area $10-100$ times larger than current telescopes. Due to the special design of nested grazing-incidence optics, the mass constraints of the telescope and economic considerations, these goals are difficult to achieve and the overall production of high-quality mirrors remains a challenging field.[4] It requires thin lightweight mirrors with very

Further author information: (Send correspondence to Heng E. Zuo)
Heng E. Zuo: E-mail: zuoh@mit.edu; Telephone: (617)803-9960; Address: 70 Vassar St. 37-411, Cambridge, MA, USA 02139.

Optics for EUV, X-Ray, and Gamma-Ray Astronomy VIII, edited by Stephen L. O'Dell, Giovanni Pareschi, Proc. of SPIE Vol. 10399, 1039910 · © 2017 SPIE · CCC code: 0277-786X/17/$18 · doi: 10.1117/12.2274273

good surface figure accuracy, which are difficult to fabricate with traditional commercial methods. Current x-ray telescope technologies are still quite limited in sensitivity and resolution, which limits our ability to study astrophysical phenomena in fine detail.

Over the past 16 years, NASA's Chandra X-ray Observatory has provided an unparalleled means for exploring the high energy universe with its half-arcsecond angular resolution. Chandra studies deepen people's understanding of galaxy clusters, active galactic nuclei, normal galaxies, supernova remnants, planets, and solar system objects, as well as advancing our understanding of dark matter, dark energy, and cosmology. The key to Chandra's success is its 0.5 arcsecond resolution, but it's also clear that many Chandra observations are photon-limited.[5] A successor to Chandra with comparable angular resolution and greatly increased photon throughput is the Lynx Mission, a large strategic mission concept which will host an x-ray telescope with an effective area of more than $2\,m^2$ at an x-ray energy of 1 keV, and a 15 arcminute field-of-view with 1 arcsecond or better half-power diameter resolution.

1.2 Contact slumping for NuSTAR mirrors

Traditional grinding and polishing techniques for shaping thick optics do not work well for ultra thin optics in x-ray telescopes, because thin optics suffer excessive deformation and stress under grinding, which leads us to seek novel methods for manufacturing thin mirror substrates. Up to now, people have devised primarily four fabrication technologies which have successively promoted the progress towards high-resolution x-ray telescopes, including electroplated nickel-cobalt replication,[6] silicon pore optics,[7] slumped glass,[8–10] and polished single-crystal silicon.[11]

NASA Goddard Space Flight Center (GSFC) developed a method called "slumping" wherein thin glass sheets are placed onto high precision mandrels to form into desired Wolter type mirror figures by thermal shaping. This method has successfully fabricated mirrors for the NASA NuSTAR telescope with good fidelity at long spatial wavelengths ($> 50\,mm$). However, the mirrors generated by this process are limited to resolution of about 6.5 arcsecond HPD with a pair of mirror segments (when properly aligned and assembled),[12] primarily due to mid-range scale spatial frequency errors. The cause of these mid-range errors is believed to be dust or particles in the anti-stick coatings used to prevent adhesion of mandrels and mirrors. Another downside is caused by the thermal asymmetry between two surfaces of the glass — on one side the glass is contacting air, while on the other side it is touching the solid mandrel — which limits the glass cooling rate in order to minimize temperature gradients and to avoid curling the mirror. Thus the total thermal cycle is long ($> 50\,h$) for each piece of mirror to ensure success of the shaping process.

1.3 Non-contact air-bearing slumping

Considering the low long-range spatial frequency error potential as well as the unresolved mid-range frequency errors that contact slumping endures, we have devised the idea of non-contact slumping using porous air-bearings, which potentially could produce thin-shell mirrors with low mid-range spatial frequency errors, and with lower cost mandrels and quicker processing time, which could result in significantly reduced manufacturing costs.[13]

In non-contact slumping, a pair of porous mandrels allows air to pass through and creates two thin layers ($15-50\,\mu m$) of air flow. The mirror sits between the two thin air films, supported by the viscous creeping flow of air. The system is then heated to a temperature slightly higher than the glass strain point, resulting in low enough viscosity to allow the glass to replicate the mandrel figure without direct contact with the mandrel surface. Figure 1 depicts the non-contact air-bearing slumping process.

Since air flow can sweep away dust particles, and the air film thickness is larger than the typical dust particle size in a clean room environments (less than $10\,\mu m$), mirrors are not expected to trap these particles. In addition, the medium on both sides of the glass is the same — air (plus bearing), with the same thermal mass, which exhibit the same heating and cooling rates, resulting in a very high degree of thermal symmetry, thus enabling much more rapid slumping cycles.

Stress relaxation during the slumping process

The success of slumping is very much dependant on the stress relaxation of the glass sheets. From a raw substrate to a formed mirror, we not only want the glass to replicate the desired shape, but also need to relieve

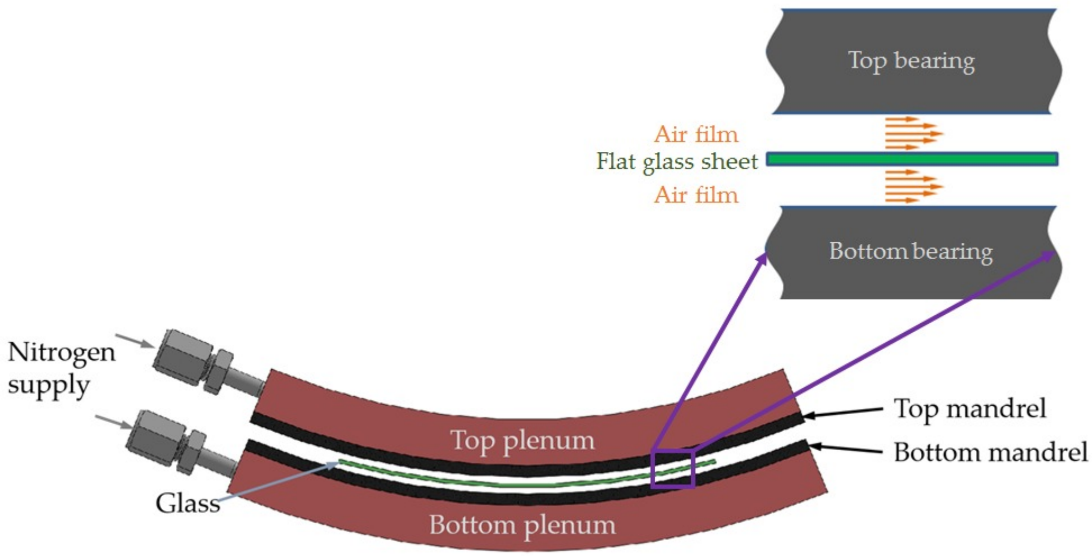

Figure 1: Illustration of air bearing slumping process (not drawn to scale). A hot glass sheet is supported by two cushions of thin air films created by opposing porous air bearings.

the internal stress inside the glass, so it won't deform further after external forces are removed. Annealing is a process of slowly cooling hot glass objects to relieve residual internal stresses introduced during manufacture. As the temperature increases, glass will soften and transit from a hard and relatively brittle state into a viscous state. During this process, its liquid viscosity decreases while its fluidity increases.

The glass-transition temperature is characterized by a range of temperatures over which this glass-to-liquid transition gradually occurs. Within this range, the glass is still hard enough to take on significant external deformation without fracture, but it is also soft enough to relieve internal strains through internal microscopic flow. To describe the glass transition phenomenon, several conventions are defined by either a constant cooling rate (for instance $20\,K/min$), or a viscosity threshold (for instance $10^{12}\,Pa \cdot s$). The Williams-Landel-Ferry model[14] is used to describe the temperature dependence of the liquid viscosity of materials that have a glass transition temperature:

$$\mu(T) = \mu_0 \exp\left(\frac{-C_1(T-T_r)}{C_2+T-T_r}\right) \tag{1}$$

where T is temperature, T_r is a reference temperature related to the glass transition temperature T_g, and C_1, C_2 and μ_0 are empirical parameters with only two of them being independent. These parameters are determined by fitting of discrete values through experiments for different materials.

The substrate material we use for slumping tests is Schott D263, a colorless borosilicate glass manufactured through a special down-draw method. Some of the technical details for this material are shown in Table 1.

Thermal cycles

The stress relaxation of glass leads us to the design of thermal cycles. Typically there are three stages in a cycle: ramping, dwelling, and cooling. Considering the long-term durability of our slumping tool, as well as the minimum requirements for glass transition, we want to operate our system at a relatively low temperature above the glass strain point. We used $550°C$, considerably lower than other groups doing contact slumping, which typically have glass slumped around $600°C$. For this reason, we need to dwell at our peak temperature longer as compared to other groups, and we have tried to tune the dwell time in the range of $0.1-100\,h$.

Figure 2 shows the readings from thermocouples in one of our experiments. Compared to the $50\,h$ typical of contact slumping time, we could significantly reduce the cooling time in non-contact slumping.

Quantity	Temperature	Corresponding viscosity	Explanations
Strain Point	$529°C$	$10^{13.5}\,Pa \cdot s$	Transition starts here. Below this point fracture occurs before plastic deformation. Internal stresses could be relieved within a few hours at this point.
Annealing Point	$557°C$	$10^{12}\,Pa \cdot s$	Atomic diffusion is sufficiently rapid to remove any internal stresses within a few minutes at this point.
Softening Point	$736°C$	$10^{6.6}\,Pa \cdot s$	Maximum temperature at which glass could be handled without causing significant dimensional alterations.

Table 1: Key temperature points for Schott D 263 glass.[15]

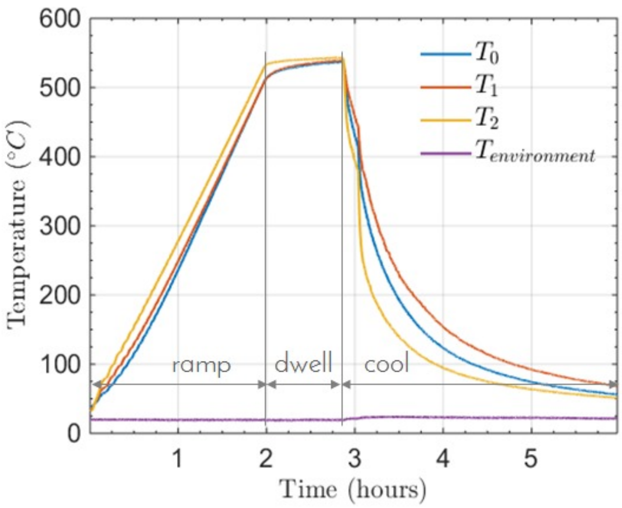

Figure 2: Typical slumping thermal profile. There are only three stages in air-bearing slumping. The symmetric thermal design allows for much shorter cooling time and slumping cycles.

2. RECENT SLUMPING RESULTS

We performed a series of slumping experiments with different dwell times ($\leq 1\,h$) and observed the change of surface profiles of the slumped glass. The idea is to explore whether there is a repeatable "steady state" in the air-bearing slumping process, and if it exists, what experimental parameters are needed to reach it.

2.1 Exploring different slumping times

We used round flat Schott D263 glass wafers of $100\,mm$ diameter and $550\,\mu m$ thickness. A Shack-Hartmann tool[16] was used to measure the surface topography of substrates. Figure 3 shows an un-slumped substrate with a large surface waviness, typically with P-V of $60-90\,\mu m$ and large slope errors with strong asymmetries between the axes. A large bow shape presents itself along one direction of the substrate with > 200 arcsecond RMS slope.

Initially, we performed a series of slumping experiments with short dwell time ($\leq 1\,h$). The results are shown in Figure 4. We noticed similar slumping results for different substrates under the same slumping conditions after the same slumping time, given that the initial shape of these substrates were also similar. In the figure, each point represents a different piece of glass.

In Figure 4, the left graph shows the reconstructed surface P-V of slumped samples after a series of dwell times between $0.1-0.9\,h$. We observed a P-V decrease with increasing slumping time, especially in the first $0.5\,h$, with the rate of this decrease slowing down after $0.5\,h$. The right graph shows the reconstructed surface profile after $0.5\,h$ of dwelling. Though the P-V has significantly decreased, there is still strong astigmatism that has not been fully removed from the un-slumped substrate, which possibly indicates insufficient dwell time.

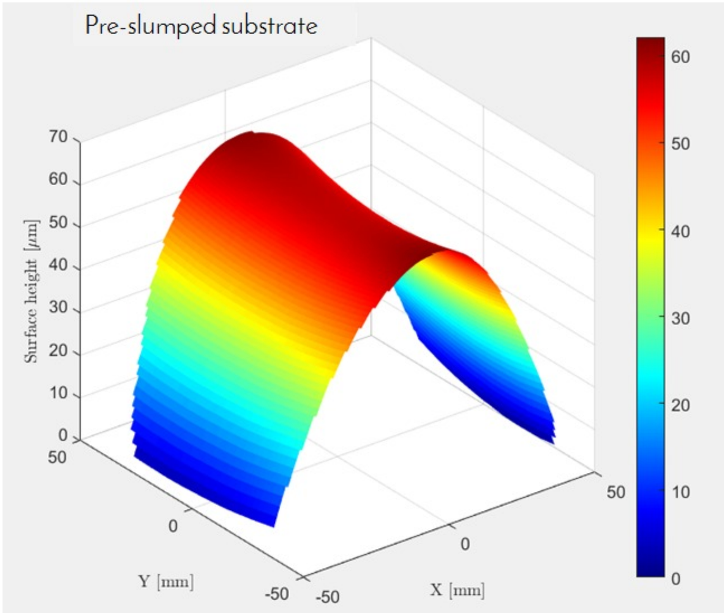

Figure 3: Reconstructed surface of a typical D263 substrate before slumping exhibits strong asymmetries between two axes: the X axis exhibits a strong curvature with a 275 arcsecond RMS slope; the Y axis is flatter with a 22 arcsecond RMS slope.

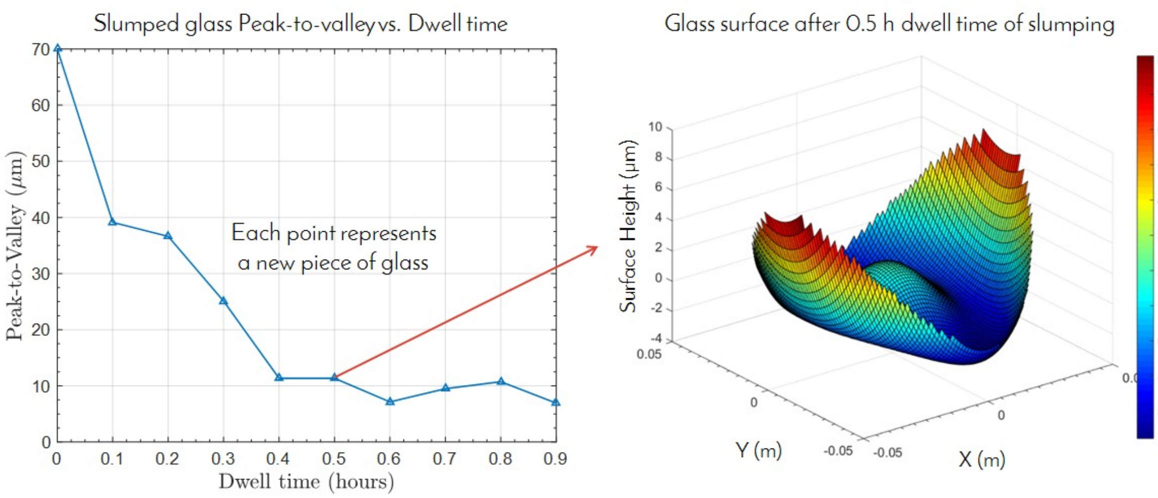

Figure 4: Short dwell experiments. Left: reconstructed surface P-V of slumped samples after a series of dwell times between $0.1 \sim 0.9\,h$. Right: Example of reconstructed surface profile after $0.5\,h$ dwell time.

2.2 Trying to establish a repeatable "steady state"

Having noticed the constant decrease of P-V with increasing slumping time, we were interested if this trend would keep decreasing as we slump longer. We carried out some long dwell time slumping experiments to find out if an assumed steady state shape could be reached.

Figure 5 shows two slumping results after $16\,h$ of dwelling. The two surface profile have similar P-V of $\sim 15\,\mu m$ and similar "sombrero" shape, with a dome in the center and slight curls at the rims. It is interesting that even though we have increased the dwell time, the P-V of the slumped glass became larger again, and the surface profile looks quite different from that of the short slumping experiments.

We slumped a few substrates with even longer dwelling times. Figure 6 shows two slumping results after $100\,h$ of dwelling. The two surface profiles have similar P-V of $\sim 20\,\mu m$ and similar "water fountain" shape, with a dome in the center and obvious curls at the rims.

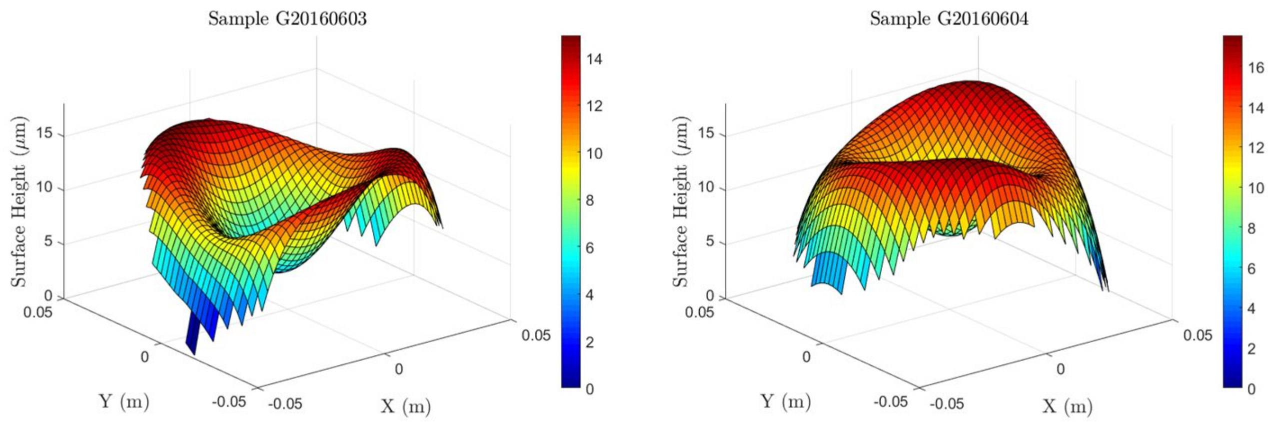

(a) (b)

Figure 5: Two experiments of long dwell time ($16\,h$). Note similar surface profiles with P-V of $15\,\mu m$.

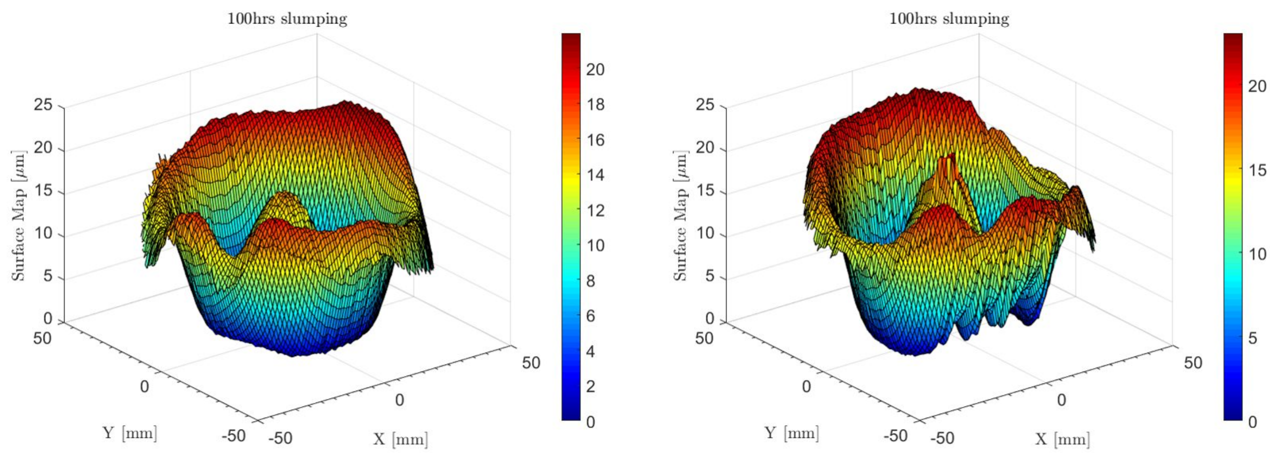

(a) (b)

Figure 6: Two experiments of long dwell time ($100\,h$). Note similar surface profiles with P-V of $20\,\mu m$.

This raises an interesting question: Why can we not seem to reach a repeatable steady state shape after such long slumping times? Is there convergence to a certain shape at all? In order to further understand the underlying mechanism of the slumping process, especially how the glass moves and deforms, we decided to develop a computer model as described in the following section.

3. NUMERICAL MODELING AND ANALYSIS

The purpose for conducting numerical modelling and analysis is to analyze the dynamic deformation and motion of the glass under the influence of air flow. The problem has several challenges:

1. Two systems — fluid (air films) and the structure (glass) — are interacting with each other;
2. Three sets of equations — porous air flow in the bearing, creeping air flow in the gap, and structural change of the glass — are tightly coupled;
3. The mechanical and thermal models of the glass have not been fully established.

Figure 7 shows the coupling of air flow and glass. The porous air flow in the bearing drives the creeping air flow in the gaps between bearings and the glass. This creeping air flow then interacts with the glass through fluid-structure interaction (FSI). The induced structural change of the glass then reflects back to the porous air flow.

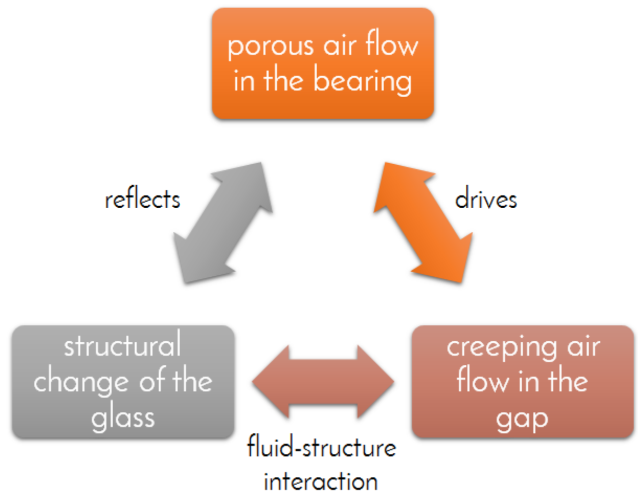

Figure 7: The porous air flow in the bearing, creeping air flow in the gap, and structural change of the glass are all tightly coupled.

3.1 Fluid-structure interaction (FSI)

FSI can solve the problem when fluid flow causes deformation of the structure, while this deformation, in turn, changes the boundary conditions of the fluid flow. To solve the coupling between the fluid and the structural models, the conditions of displacement compatibility and traction equilibrium along the structure-fluid interfaces must be satisfied:

Displacement compatibility: $\mathbf{d}_f = \mathbf{d}_s$ (2)

Traction equilibrium: $\mathbf{n} \cdot \tau_f = \mathbf{n} \cdot \tau_s$ (3)

where $\mathbf{d}_f$ and $\mathbf{d}_s$ are the fluid and solid displacements, respectively, τ_f and τ_s are the fluid and solid stresses, respectively, and $\mathbf{n}$ is the local normal direction of the fluid-solid interface.

As stated before, the glass deformation is rooted in its interaction with the air flow, and can be modeled with FSI. This assumes no absolute displacement change of the glass. On the other hand, the cause for any glass motion is essentially a force imbalance. The forces exerted on the glass are the net pressure from the surrounding air and the gravity of the glass. If the net force exerted on the glass is non-zero, then the glass has a total displacement along the direction of the net force. This assumes there is no deformation in the glass, such that the glass is moving as a rigid body pushed by the ambient air flow.

In this problem, the fluid field and FSI have different time scales: the disturbance in the fluid field can incur immediate response, yet the viscoelastic deformation in the glass takes a much longer time. So it is possible to separate the simulation of glass shape (deformation through FSI) and glass position (motion through fluid mechanics of air), and we used an iterative scheme as shown in the following recipe:

Iterative Scheme

1. Assuming the glass is a rigid body, perform computational fluid mechanics (CFD) in the air films to find the force balance position of the glass:
   - Conduct CFD simulation, calculate total force on the glass

     $$F_{total} = \int_{\Omega} (p_{top} - p_{bottom}) dA \; + \; \rho g h A; \tag{4}$$

     where p_{top}, p_{bottom} are the pressure from the top and bottom glass-air interface, ρ, h, A are the density, thickness and surface area of the glass, respectively, and g is the gravitational constant.
   - If $F_{total} > 0$, there is a net force pointing downwards, then move the glass position towards the bottom, and vice versa.
   - Repeat above two steps until the net force on the glass is close to zero within a threshold, then maintain the position of the glass.

2. Maintain the same glass position from Step 1 and deform the glass using fluid-structure interaction:

- Conduct FSI simulation for a certain length of time (controlled by the relaxation time of the viscoelasticity of glass, which is explained in the next section).
- Calculate the deformation of the glass and update the shape of the glass.

3. Iteratively perform the above two steps, with enough iterations to approximate the actual physical time.

The advantage of this scheme is that it not only considers the macro force balance of the glass (in Step 1), but also leaves enough time for stress relaxation within the glass (in Step 2).

3.2 2D axisymmetric viscoelastic glass model

To simplify the complexity of the problem and to proceed with the simulations, we made the following assumptions:

1. A 2D axisymmetric model is considered, where the solution variables are the same on each radial cross-section plane in a cylindrical coordinate system. Therefore solutions can be defined in a domain on one radial plane, and the glass center is pinned laterally at the bearing center.
2. The glass can be treated as a viscoelastic material.
3. Only the dwell stage is simulated, so constant temperature and air parameters are used.
4. The influences of air-bearing permeability are considered, and non-uniform permeability can be enforced.
5. The gravity of the glass can be either included or excluded to study its influence on the glass deformation.

It's worth noticing that the 2D axisymmetric model imposes that the vertical displacement of the glass center (along the axis shown in Figure 8) should be continuous, as well as its first order derivative. As a result, there cannot be any nonzero moment or torque applied on the substrate. This is why no rigid body bending is considered in Step 1 of the Iterative Scheme 3.1.

The simulation results with an elastic glass model have been discussed in previous work.[17] Here we introduce a new model for viscoelastic materials. Unlike elastic materials which can deform back to the original state very quickly once the stress is removed, viscous materials show resistance to shear flow and strain linearly with time under external stress. Glass above its strain point can be viewed as a viscoelastic material, exhibiting both viscous and elastic characteristics when undergoing deformation. The strain is time-dependent, as a result of the diffusion of atoms or molecules inside an amorphous material.

The stress-strain relationships for the linear viscoelastic materials* are:

$$\sigma'_{ij}(t) = 2G(t)\epsilon'_{ij}(0) + \int_0^t 2G(t-\tau)\dot{\epsilon}'_{ij}(\tau)d\tau \tag{5}$$

$$\frac{1}{3}\sigma'_{ii}(t) = K(t)\epsilon'_{kk}(0) + \int_0^t K(t-\tau)\dot{\epsilon}'_{kk}(\tau)d\tau \tag{6}$$

where σ is the stress, ε and $\dot{\varepsilon}$ are the strain and time derivative of strain respectively, τ is the relaxation time, and t is the physical time. The shear modulus $G(t)$ and bulk modulus $K(t)$ can be modeled as Prony series:

$$G(t) = G_\infty + \sum_{i=1}^{N} G_i\, e^{-\frac{t}{\tau_i^G}}, \tag{7}$$

$$K(t) = K_\infty + \sum_{i=1}^{N} K_i\, e^{-\frac{t}{\tau_i^K}}, \tag{8}$$

where there are N elements with moduli E_i, viscosity $\eta_i^G,\ \eta_i^K$, and relaxation times $\tau_i^G = \frac{\eta_i^G}{E_i},\ \tau_i^K = \frac{\eta_i^K}{E_i}$.

The model is set up as shown in Figure 8. It is a 2D axisymmetric model with the glass center pinned laterally at the bearing center. The top and bottom bearings are divided within the radius of the glass into 50 regions with variable permeability along the radial direction. Constant pressure is supplied to the system from the pair of surfaces as indicated by the pink arrows.

*Linear viscoelastic materials exhibit linear stress-strain relationships at any given time. Linear viscoelasticity provides a reasonable engineering approximation for many materials at relatively low temperatures and under relatively low stress, and this theory is usually applicable for small deformations.

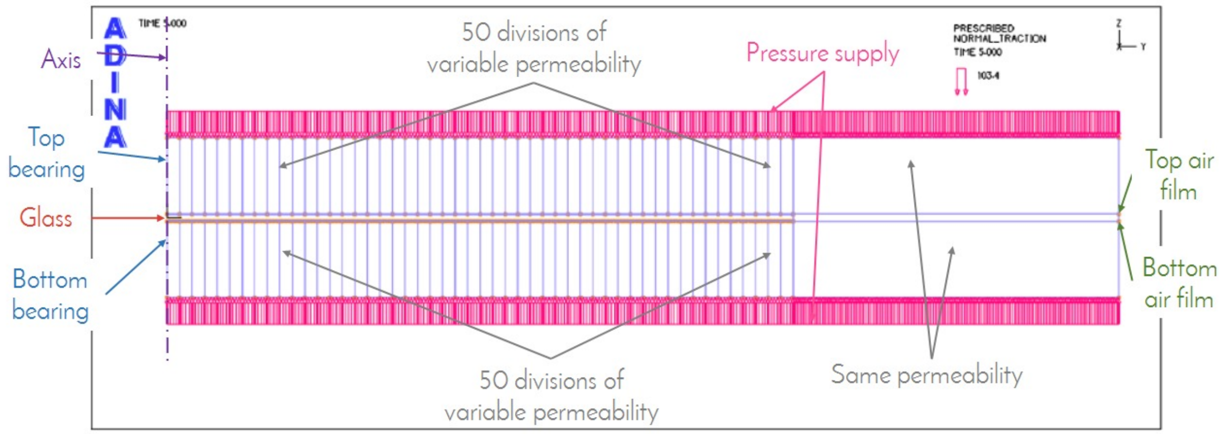

Figure 8: 2D axisymmetric model with variable air-bearing permeability along the radial direction.

Material properties used for this model were: For glass — Young's modulus $E = 72.9\,GPa$, Poisson's ratio $\nu = 0.208$, density $\rho = 2.51\times10^3\,kg/m^3$, relaxation time $\tau = 13.7\,s$, viscosity $\eta = 10^{12}\,Pa{\cdot}s$; For air — viscosity $\mu = 3.623\times10^{-5}\,kg/(m{\cdot}s)$, density $\rho = 0.4027\,kg/m^3$; For the air-bearings — average permeability $\kappa = 4\times10^{-13}\,m^2$. Geometric properties used for this model were: For glass — radius $50\,mm$, thickness $550\,\mu m$; For air film — total thickness (adding air films on both side of the glass) $100\,\mu m$; For the air-bearings — radius $72\,mm$, thickness (of each bearing) $6\,mm$.

3.3 Results showing there appears to be no "steady state"

With the above model, we started with an arbitrary glass shape input and performed many iterations as shown in section 3.1, observing progression of the glass shape as well as the von Mises stress† in the glass.

Figure 9 shows how the scheme updates the shape and position of the elastic glass through iterations. In Fig.9a, each line represents the simulated glass shape after one iteration, each iteration corresponding to a certain physical time ($10\,s$). The blue line shows the initial input shape, and the green line shows the output shape after 230 iterations. In Fig.9b the RMS von Mises stress of the glass drops dramatically after a few iterations, then climbs up by a small amount followed by a gradual decrease.

Figure 10 shows the same simulation of Figure 9 extended to 850 iterations. In Fig.10a, with more iterations, the glass deforms even further, a second lobe forming closer to the central axis. In Fig.10b, the von Mises stress tends to maintain a relatively constant value as the iteration number increases. The increasing number of lobes in the deformed glass, and the apparent plateauing of the von Mises stress to a constant non-zero value, suggests an inability of the model to converge to a steady state. We have experimentally observed an increasing number of lobes with slumping time (see Figures 5 and 6), shapes similar to the modelling results shown in Figure 10. The reasons for the increasing number of lobes are not fully understood and will require further modelling and analysis.

After conducting many similar simulations, we have found that as long as the differences in the input initial shape of the glass are not too great (P-V within $\pm5\,\mu m$), after a few number of iterations the output glass shape will be very similar. From these observations, we infer that there seems to be no convergence of the glass shape, i.e. no "steady state". In addition, the initial glass shape seems to be not very critical to the simulation results; and it is the slumping time that determines the shape after a certain number of iterations.

† Von Mises stress, also known as the equivalent tensile stress, is directly related to the deviatoric strain energy and describes yielding of materials.

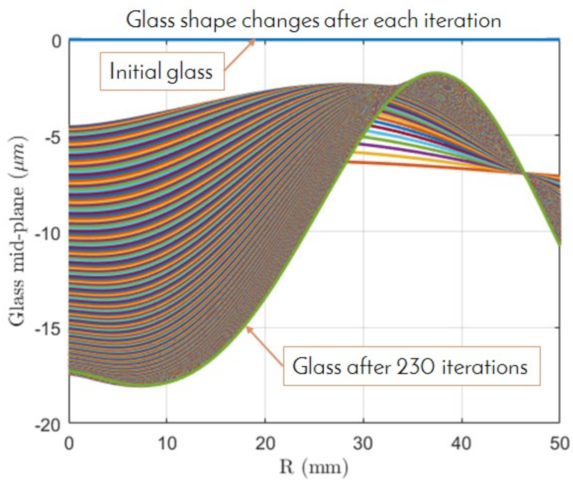

(a) Evolution of the glass through iterations. Blue line: input initial glass. Green line: output glass after 230 iterations.

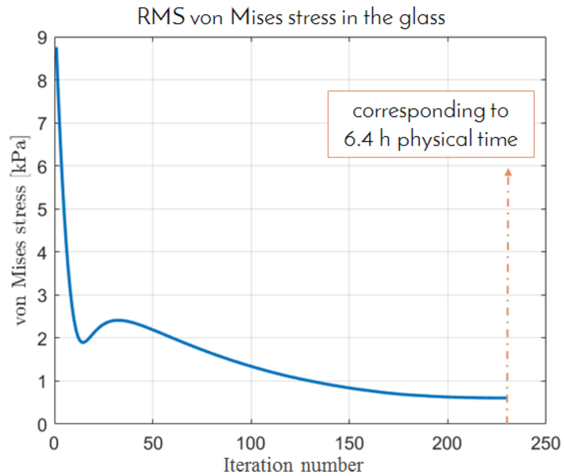

(b) RMS deformation of the glass between successive iterations.

Figure 9: Simulation results after 230 iterations.

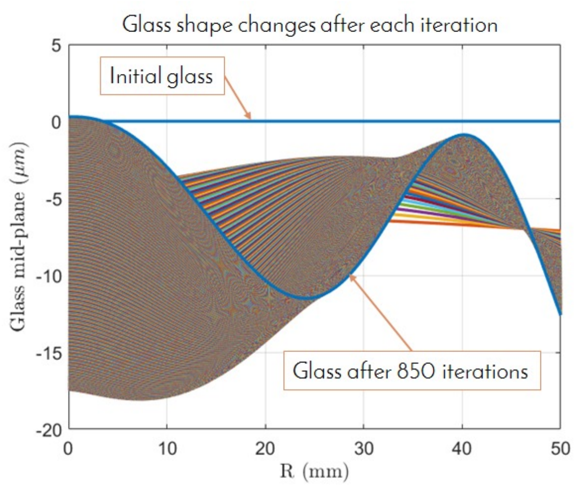

(a) Evolution of the glass through iterations. Blue line: input initial glass. Dark blue line: output glass after 850 iterations.

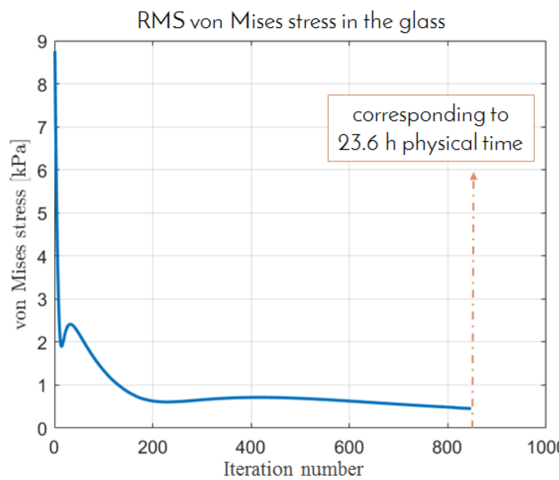

(b) RMS deformation of the glass between successive iterations.

Figure 10: Simulation results after 850 iterations.

4. COMPARING SIMULATIONS WITH EXPERIMENTS

After obtaining results from both experiments and simulations, we compared them to evaluate the suitability of our approach.

4.1 Comparing experiment and simulation results

Figure 11 compares the result of the 2D axisymmetric simulation with the measured surface of slumped glass sample G20160604 shown in Figure 5. The circles are surface height data from the slumped glass at every measured grid point. The circles do not make a single curve because the surface profile of the glass is not fully axisymmetric and has strong astigmatism. The line represents the simulated surface profile at a pressure supply of $0.025\,psi$ (same as the experiment) after 90 iterations (corresponding to $2.5\,h$ physical time).

This figure shows that simulation and experiments could produce comparable results. However, the experimental data was taken from a sample slumped for $16\,h$, while the numerical data was from a simulation corresponding to $2.5\,h$ physical time. This discrepancy is suspected to be caused by the different initial shape for the experiment and simulation. For most experiments, we started with a very curved glass with $90\,\mu m$ P-V, while in the simulation we assumed the initial shape to be flat. Since the initial shapes are rather different, the time to reach the same output shape might also be quite different.

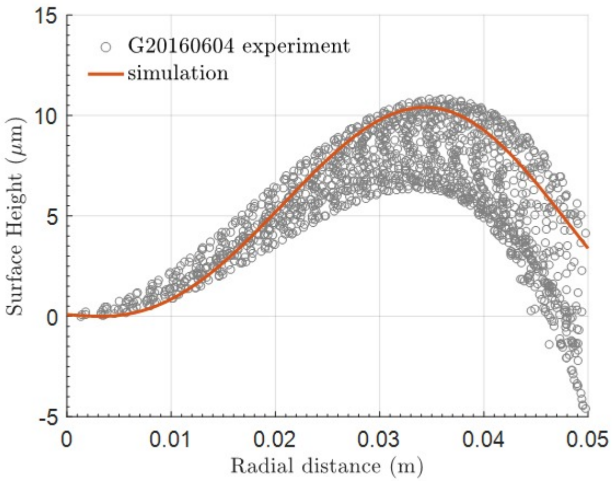

Figure 11: Comparison between the 2D axisymmetric simulation result with the surface measurements of slumped glass sample G20160604. The dots are scattered surface profile data at grid points from the slumped glass. The line represents the simulation result after 90 iterations (corresponding to 2.5 h physical time).

4.2 Effect of non-uniform bearing permeability

The permeability over porous silicon carbide is typically around $10^{-15}\,m^2$, while the permeability of carbon graphite can vary between 0.07–$10 \times 10^{-15}\,m^2$. Since bearing permeability directly affects the pressure distribution in the gap and controls the final slumping result, the measured value and uniformity of the actual bearing permeability are of critical importance.

We measured the bearing permeability of both the SiC and graphite bearings by measuring the local flow rate from the bearing surface. Continuous air flow with constant pressure was fed into the bearing through the air inlet on the backside, and a plastic tube was applied on the bearing side, with an inner diameter of $0.1\,in$ connecting to a flowmeter. The reading of the flowmeter was then recorded, which indicated the total flow rate inside the tube. The bearing surface was meshed into small squares of size $0.1\,in \times 0.1\,in$ to match the diameter of the tube, so each time only the flow coming from one square was measured. The measurement for all squares were repeated and the bearing permeability for each square was calculated from the following formula:

$$\kappa = \frac{4\dot{V}\nu}{\pi d^2 P} \tag{9}$$

where $\dot{V}$ is the measured flow rate in volume per unit time, $\frac{\pi d^2}{4}$ is the surface area inside the tube, ν and P are the viscosity and pressure of the air supply.

Figure 12 shows the measurement results. For the flat circular porous SiC bearing, the outer rim region was coated with a layer of sealant, resulting in a permeability loss of about 50%. In the central regions where the glass floats, the permeability is on average $4 \times 10^{-15}\,m^2$. For measured cylindrical porous graphite bearings, the average permeability is about $1.1 \times 10^{-17}\,m^2$, which is much lower. While the maximum relative difference is 60% along the azimuth direction, the average difference along the radial direction is 25%.

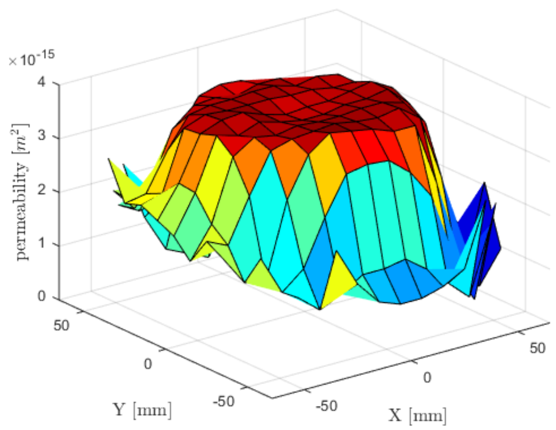

(a) Measured permeability of a flat circular porous SiC bearing. The outer rim region is coated with a layer of sealant, resulting in a permeability loss of about 50%. In the central areas, the permeability is about $4 \times 10^{-15}\ m^2$ with ±12% variation.

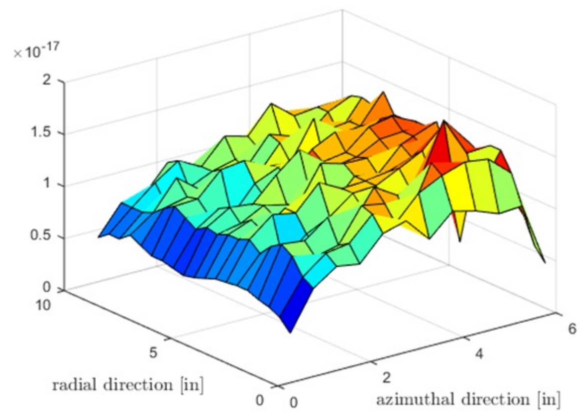

(b) Measured permeability of a cylindrical porous graphite bearing. The average permeability is about $1.1 \times 10^{-17}\ m^2$. While the maximum difference is 60% along the azimuth direction, the average difference along the radial direction is ±12%.

Figure 12: Measured permeability of bearings.

4.3 The air-bearing slumping system acts like a low-pass filter

Having noticed the variations in bearing permeability, we examined the effect of bearing permeability non-uniformity on the glass deformation. In order to simulate only the influence of varying permeability, we excluded the weight of the glass for the following simulations.

Using our FSI model as described in the previous section, multiple different input bearing permeability profiles were tested and the shapes of the glass after the same number of iterations were recorded. As a sanity check, we input identical top and bottom bearing permeability of different distributions. The results are shown in Figure 13, where the input permeability is shown on the left, and the output glass surface profiles are shown on the right. The input permeability distributions from top to bottom are uniform, linear and quadratic distributions. The output glass deformation should be zero in theory, yet these figures all show a P-V value of roughly $0.05\,nm$ after 200 iterations. This mismatch is believed to be caused by numerical errors, i.e. any initial numerical errors would cause the glass to deform in a certain way, but the magnitude should not exceed $0.05\,nm$.

Following this, we performed another test by disturbing the permeability in only one cell of the top bearing at different radial locations, while maintaining the same permeability everywhere else. Figure 14 presents the results of this test. Each row shows one case with a "bump" in the top bearing permeability at different locations. The left column shows the profile of bearing permeability, while the right column shows the surface profile of the resulting glass.

In all three cases, the magnitudes of the disturbed bearing permeability in the "bump" are the same (25% higher), and the output P-V values in glass are also very comparable of around $0.11\,\mu m$. These modelling results show that a variation in the bearing permeability will imprint on the glass shape: the peak in the resulting glass shape is found at approximately the same place of the permeability variation, but the width of the glass deformation is significantly larger than the width of the permeability variation. This suggests that air-bearing slumping should be able to smooth out high spatial frequency variabilities in the glass.

We also performed a test with random bearing permeability in all 100 cells. We took the Fourier transform of both input bearing permeability and output glass surface profile, and calculated the transfer function. The results are shown in Figure 15. (a) The bearing permeability in each cell was generated by a random function with maximum ±12.5% difference from the average permeability. (b) The output is a smooth curve with P-V

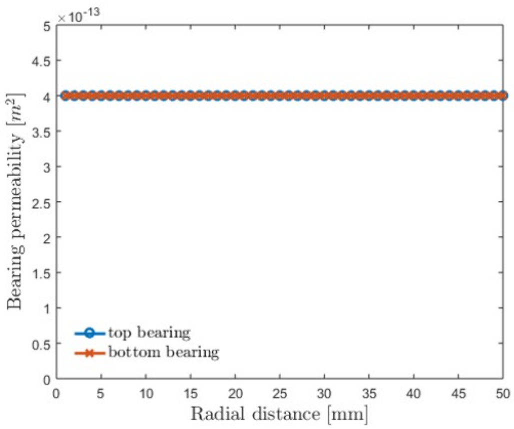

(a) Input uniform permeability distribution.

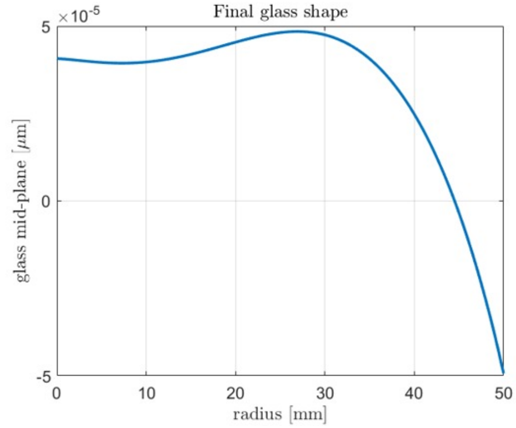

(b) Output glass shape of (a).

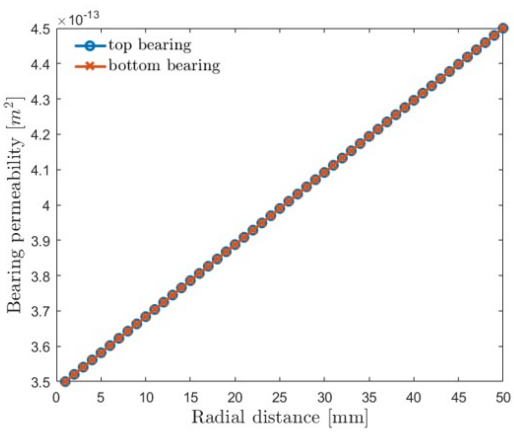

(c) Input linear permeability distribution.

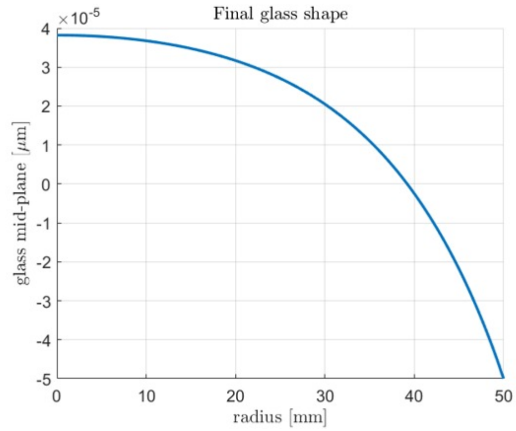

(d) Output glass shape of (c).

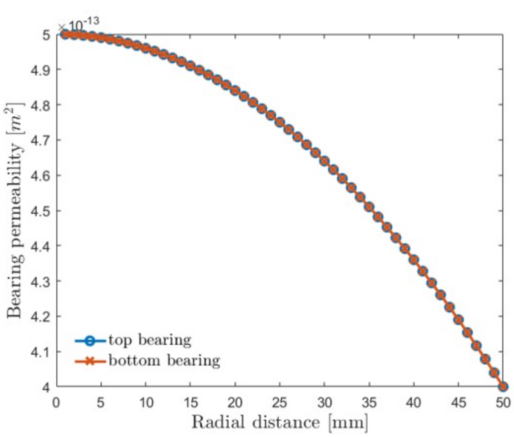

(e) Input quadratic permeability distribution.

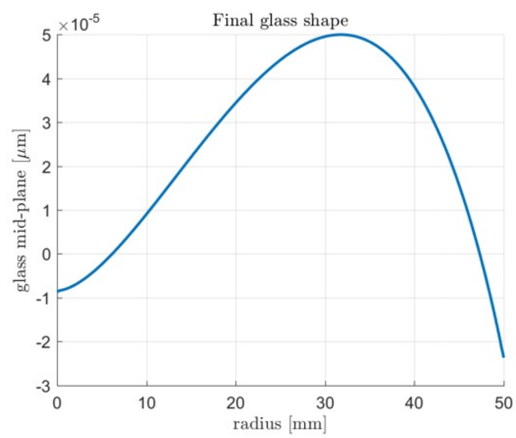

(f) Output glass shape of (e).

Figure 13: Numerical model sanity check: Assuming identical top and bottom bearing permeability of different distributions creates output glass surface P-V of only about $0.05\,nm$. Input bearing permeability distributions are shown on the left, the output glass surface profiles on the right.

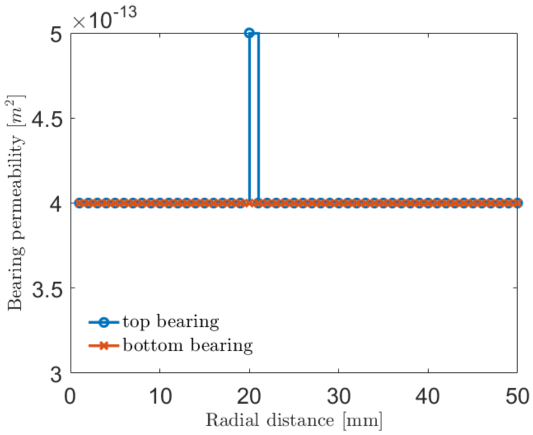

(a) Input permeability "bump" at 20 mm.

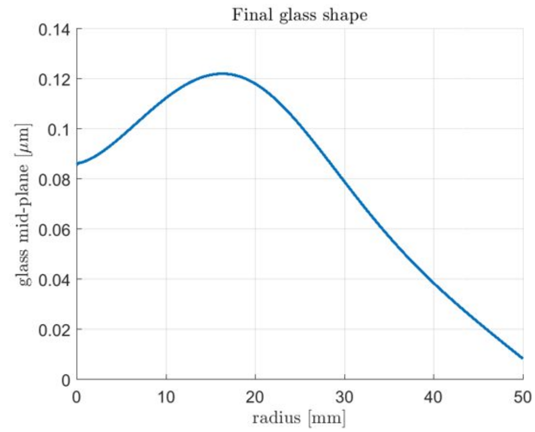

(b) Output glass shape of (a).

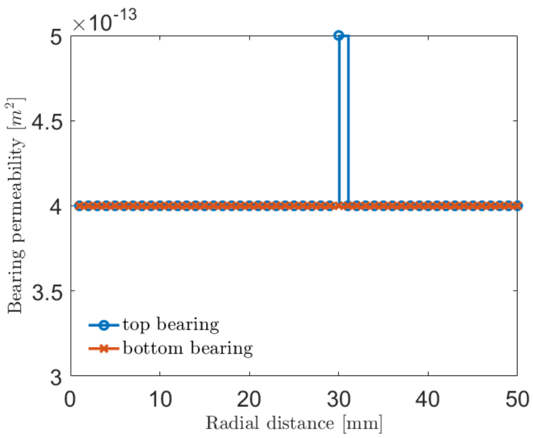

(c) Input permeability "bump" at 30 mm.

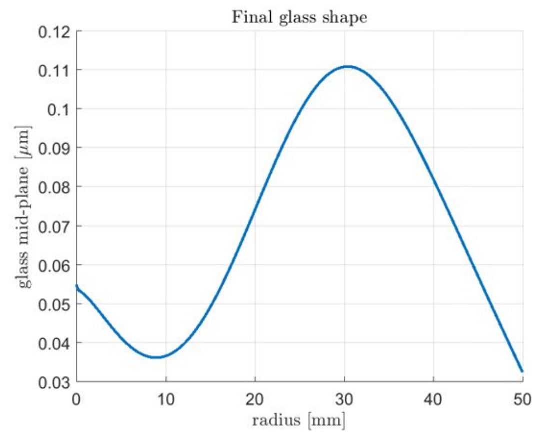

(d) Output glass shape of (c).

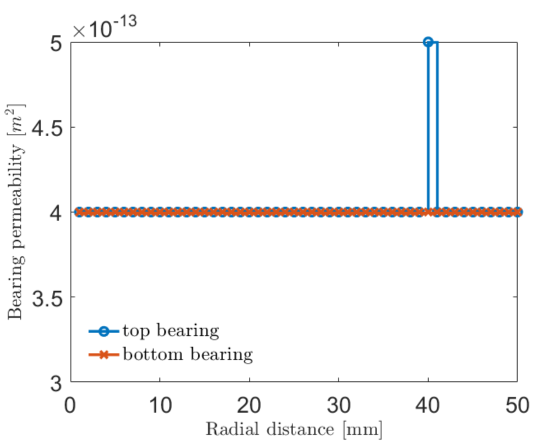

(e) Input permeability "bump" at 40 mm.

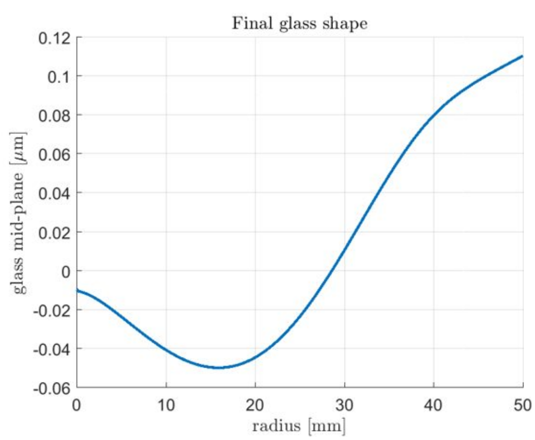

(f) Output glass shape of (e).

Figure 14: Results of an artificial "bump" in the input top bearing permeability of identical magnitude at three different locations. Input bearing permeability distributions are shown on the left, the resulting glass surface profiles on the right.

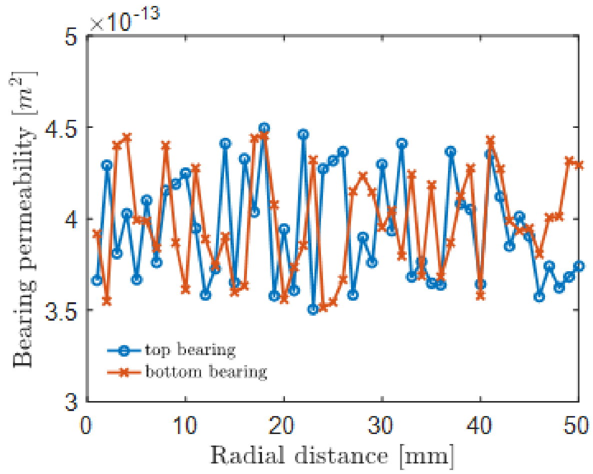

(a) Input random bearing permeability.

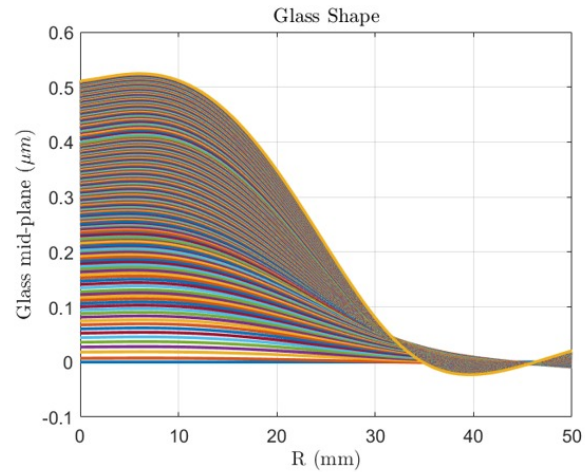

(b) Output glass deformation after 200 iterations.

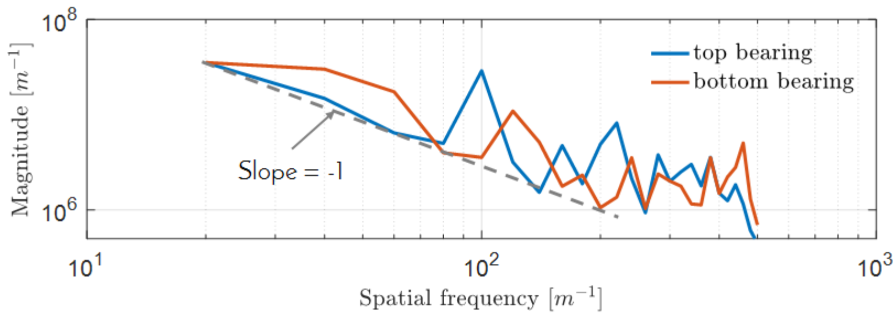

(c) Transfer function of permeability non-uniformity to glass deformation.

Figure 15: Results of input normally distributed bearing permeability.

around $0.5\,\mu m$. (c) The transfer function from the bearing permeability non-uniformity to glass deformation shows that the air-bearing system acts like a low-pass filter, and the fitted line has a slope approximately -1, very close to a standard linear low-pass filter.

From these results, we found that high frequency terms ($> 100\,m^{-1}$ or $< 10\,mm$) have been smoothed out, while lower frequency terms ($\leq 100\,m^{-1}$ or $\geq 10\,mm$) dominated the output results. This also shows that air-bearing slumping is capable of removing non-uniformity on the order of millimeter wavelength, thus removing mid-range spatial frequency errors in the slumped glass. In addition, a 25% variable noise in the input bearing permeability only creates a P-V of about $0.5\,\mu m$ in the glass surface after 200 iterations, which should be correctable through ion implantation.[18]

Another important result is that gravity plays a strong role in deforming the glass. After removing gravity in the above examples, the P-V of the simulated glass shape was reduced from $15\,\mu m$ with gravity to $\sim 1\,\mu m$ without gravity. This suggests one should use a vertical slumping design instead of the original horizontal slumping design in our experiments, to eliminate gravity influence and produce better surface profiles with smaller variations.

5. VERTICAL SLUMPING TESTS

5.1 Vertical slumping design

Since the simulations have suggested that vertical slumping to eliminate gravity influence may be advantageous, we have designed a vertical slumping tool with flat SiC bearings, shown in Figure 16. The bearings are now aligned vertically through compression via three springs that sustain high temperature. The bearings are separated by Kovar shims, and the glass is suspended from a beam above the bearings with tungsten wires. The design in the SolidWorks is shown in the left, and the built set-up is shown on the right.

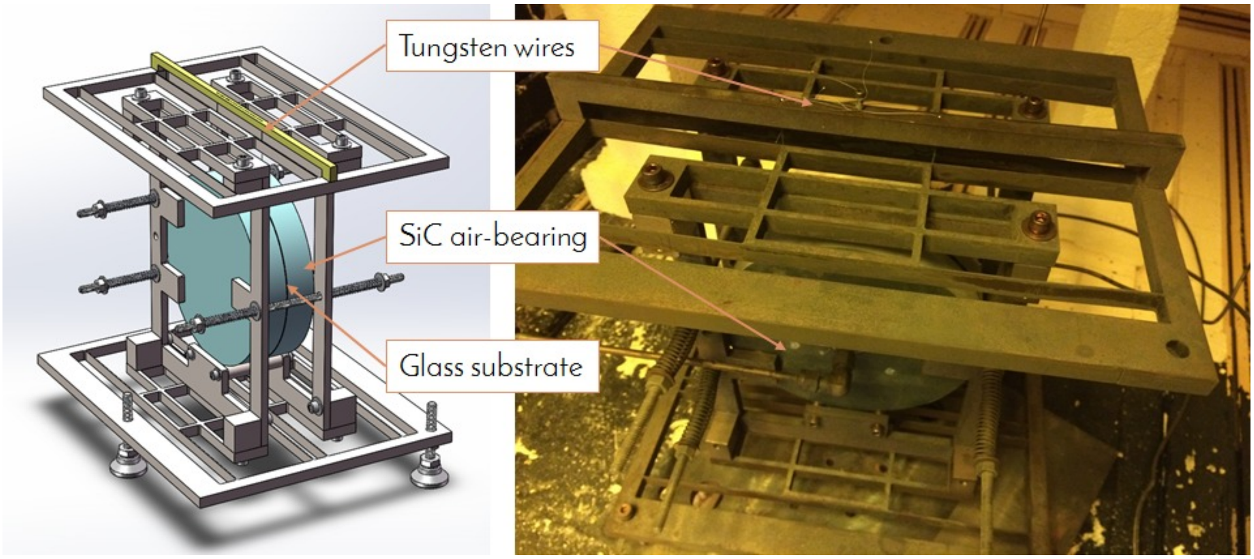

Figure 16: Vertical slumping apparatus design to eliminate gravity influence. Left: Vertical slumping design. Right: Vertical slumping experiment set-up.

5.2 Vertical slumping results

We have performed preliminary tests with several samples. Figure 17 shows the vertical slumping results of Sample G2017021601 after dwelling for 4 h. The surface P-V is measured at 15.8 μm, and the RMS slope is 58.6" in the X direction and 35.9" in the Y direction.

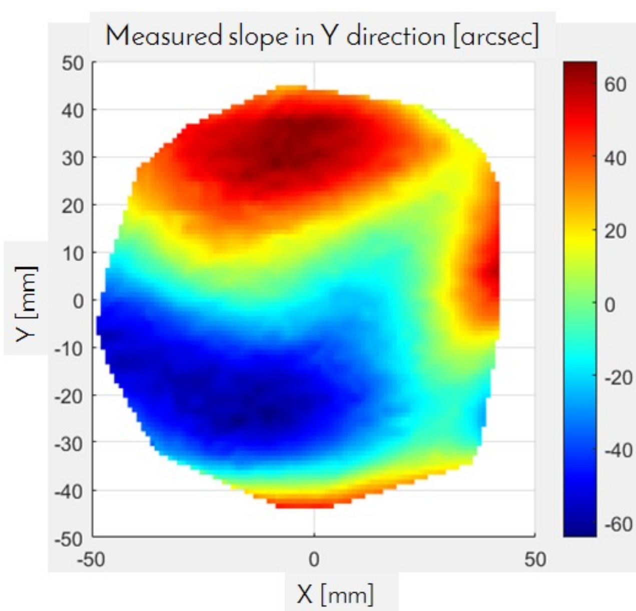

Figure 17: Surface topography of D263 wafer G2017021601 after slumping with tool shown in Figure 16 and dwelling for $4\,h$. RMS slope in the Y direction is 35.9".

We don't fully understand the reasons for the still quite large P-V, but we suspect it is caused by alignment errors. The axis of the glass may not be parallel to the direction of the gravity force in our experiments, such that the effects of gravity have not been completely removed. It is also possible that there was a considerate amount of friction between the glass and the tungsten wires, such that the glass was not able to move freely and relieve the internal stress.

Though these preliminary results are far from satisfactory, the ideal case with no gravity has been studied in the previous chapter. Given our past success to connect experiments with simulations for the horizontal slumping process, we believe vertical slumping has the potential to bring glass surface P-V down by 10 times from what we have achieved up to now.

6. SUMMARY AND NEXT STEPS

6.1 Achievements

After completing a series of experiments and simulations, the comparability between them has been established, and evidence of air-bearing slumping correcting mid-range spatial frequency errors has been identified. A deeper understanding of the mechanism behind the slumping practices has also been developed, which helps to build confidence towards our slumping system.

Our main achievements in air-bearing slumping could be summarized into the following four aspects:

- A more comprehensive understanding of the slumping mechanism has been obtained through a series of experiments and numerical analysis.
- A finite element model based on fluid-structure interaction with viscoelastic glass model has been developed, which generates comparable results with the experiments.
- The previous belief of the existence of an "equilibrium" glass shape has been proved incorrect. Therefore, considering the viscoelastic behavior of the glass, it is pivotal to control the slumping time.
- Evidence that air-bearing slumping has the ability of smoothing out system non-uniformity on the order of millimeters have been shown, thus removing mid-range spatial frequency errors in the glass.

6.2 Suggestions for future work

There is still quite a lot of room for improvement in surface quality within the realm of slumping, and we have identified a few of them.

We believe the future of air-bearing slumping is in the vertical slumping process, which, if well aligned and monitored, should be able to decrease the slumped glass surface P-V by 10 times over current best results. However, more experiments are needed to improve the stability and effectiveness of the system.

For manufacturing Wolter Type I mirrors, some 3D simulations and experiments on cylindrical slumping need to be done. And actual improvement of angular resolution from our slumped mirrors needs to be demonstrated.

Some other methods for manufacturing and correcting x-ray telescope mirrors have also produced promising results recently, and we should keep an open mind about searching for other potential alternatives as well, especially under the context of the Lynx mission.

ACKNOWLEDGMENTS

This work has been supported by NASA APRA grants NNX14AE76G and NNX17AE47G. We would also like to thank Lester Cohen of Harvard SAO for his valuable advice.

REFERENCES

[1] "Nasa Strategic Plan 2014." National Aeronautics and Space Administration, https://www.nasa.gov/sites/default/files/files/FY2014$_N ASA_S P_5 08c.pdf$ (2014).

[2] National Research Council, [*New Worlds, New Horizons in Astronomy and Astrophysics*], The National Academies Press, Washington, DC (2010). [doi: 10.17226/12951; isbn: 978-0-309-15799-5].

[3] Kouveliotou, C., Agol, E., Batalha, N., Bean, J., Bentz, M., Cornish, N., Dressler, A., Figueroa-Feliciano, E., Gaudi, S., Guyon, O., et al., "Enduring quests-daring visions (NASA astrophysics in the next three decades)," *arXiv preprint arXiv:1401.3741* (2014).

[4] O'Dell, S. L., Aldcroft, T. L., Allured, R., Atkins, C., Burrows, D. N., Cao, J., Chalifoux, B. D., Chan, K.-W., Cotroneo, V., Elsner, R. F., et al., "Toward large-area sub-arcsecond x-ray telescopes," in [*SPIE Optical Engineering+ Applications*], 920805, International Society for Optics and Photonics (2014).

[5] Weisskopf, M. C., Gaskin, J., Tananbaum, H., and Vikhlinin, A., "Beyond Chandra: the X-ray Surveyor," in [*SPIE Optics+ Optoelectronics*], 951002, International Society for Optics and Photonics (2015).

[6] Romaine, S., Basso, S., Bruni, R., Burkert, W., Citterio, O., Conti, G., Engelhaupt, D., Freyberg, M., Ghigo, M., Gorenstein, P., et al., "Development of a prototype nickel optic for the Constellation-X hard x-ray telescope: III," in [*Optics and Photonics 2005*], 59000S, International Society for Optics and Photonics (2005).

[7] Collon, M. J., Ackermann, M., Günther, R., Chatbi, A., Vacanti, G., Vervest, M., Yanson, A., Beijersbergen, M. W., Bavdaz, M., Wille, E., et al., "Making the ATHENA optics using silicon pore optics," in [*SPIE Astronomical Telescopes+ Instrumentation*], 91442G, International Society for Optics and Photonics (2014).

[8] Zhang, W. W., "Manufacture of mirror glass substrates for the NuSTAR mission," in [*SPIE Optical Engineering+ Applications*], 74370N, International Society for Optics and Photonics (2009).

[9] Zhang, W. W., Biskach, M., Blake, P., Chan, K., Evans, T., Hong, M., Jones, W., Kolos, L., Mazzarella, J., McClelland, R., et al., "Lightweight and high angular resolution x-ray optics for astronomical missions," in [*SPIE Optical Engineering+ Applications*], 81470K, International Society for Optics and Photonics (2011).

[10] Winter, A., Breunig, E., Friedrich, P., Proserpio, L., and Döhring, T., "Indirect glass slumping for future x-ray missions: overview, status and progress," in [*SPIE Optical Engineering+ Applications*], 96030S, International Society for Optics and Photonics (2015).

[11] Zhang, W. W., Chan, K.-W., Riveros, R. E., and Saha, T. T., "Toward diffraction-limited lightweight x-ray optics for astronomy," in [*SPIE Optical Engineering+ Applications*], 96030Q, International Society for Optics and Photonics (2015).

[12] Zhang, W. W., Atanassova, M., Biskach, M., Blake, P., Byron, G., Chan, K., Evans, T., Fleetwood, C., Hill, M., Hong, M., et al., "Mirror technology development for the International X-ray Observatory mission (IXO)," in [*SPIE Astronomical Telescopes+ Instrumentation*], 77321G, International Society for Optics and Photonics (2010).

[13] Schattenburg, M. L., Chalifoux, B., DeTienne, M. D., Heilmann, R. K., and Zuo, H., "Progress report on air bearing slumping of thin glass mirrors for x-ray telescopes," in [*SPIE Optical Engineering+ Applications*], 96030R, International Society for Optics and Photonics (2015).

[14] Williams, M. L., Landel, R. F., and Ferry, J. D., "The temperature dependence of relaxation mechanisms in amorphous polymers and other glass-forming liquids," *Journal of the American Chemical society* **77**(14), 3701–3707 (1955).

[15] "D263 t thin glass specifications." Präzisions Glas & Optik GmbH, https://www.pgo-online.com/intl/katalog/D263.html.

[16] Forest, C. R., Canizares, C. R., Neal, D. R., McGuirk, M., and Schattenburg, M. L., "Metrology of thin transparent optics using Shack-Hartmann wavefront sensing," *Optical engineering* **43**(3), 742–753 (2004).

[17] Chalifoux, B., Zuo, H., Wright, G., Yao, Y., Heilmann, R. K., and Schattenburg, M. L., "Gas bearing slumping and figure correction of x-ray telescope mirror substrates," in [*SPIE Astronomical Telescopes+ Instrumentation*], 99051Z, International Society for Optics and Photonics (2016).

[18] Chalifoux, B. D., Burch, C., Wright, G., Heilmann, R. K., Yao, Y., Zuo, H. E., and Schattenburg, M. L., "Effects of ion implantation in different substrate materials: stress, relaxation, and strength," in [*SPIE Optical Engineering+ Applications*], 10399–49, International Society for Optics and Photonics (2017).